RPE | Radiation Physics & Engineering
A Peer-Reviewed Journal
Published by K.N. Toosi University of Technology
http://rpe.kntu.ac.ir
Research Article

Radiation Physics and Engineering 2026; ?(?):?–?

Cluster decay half-Lives for Bh and Hs superheavy isotopes in the mass region $A = 267$–274

Mehrdad Azizi Shamami*, Mohammad Reza Pahlavani, Mohsen Saeidi babi

Department of physics, faculty of basic science, University of Mazandaran, P.O. Box 47415-416, Babolsar, Iran

HIGHLIGHTS

- Cluster radioactivity in superheavy nuclei is a quantum tunneling process and a probe of underlying nuclear structure.
- Increase in neutron number enhances the probability of heavy cluster emission while suppressing light cluster channels.
- Decay modes occur when emitted cluster and residual daughter nucleus approach magic or near-magic configurations.

ABSTRACT

This work systematically investigates the cluster radioactivity of superheavy parent nuclei ^{267,270,271,272,274}Bh ($Z = 107$) and ^{268,269,270,271,272}Hs ($Z = 108$) within a binary decay model. We consider a wide range of emitted clusters, including ^{6}He, ^{14}C, ^{18,20}O, ^{23}F, ^{22,24,25,26}Ne, ^{28,29,30}Mg, and ^{32,34}Si, along with their corresponding daughter nuclei. Using the Wentzel-Kramers-Brillouin (WKB) approximation, we compute Q-values, interaction barriers, driving potentials ($V - Q$), barrier penetrabilities, decay constants λ, and half-lives for all energetically allowed ($Q > 0$) clusterdaughter combinations. From the full set of possible emissions, we identify the most probable clusters based on the largest Q-values and significant penetrabilities. The resulting half-lives are tabulated and analyzed as a function of parent mass number, revealing systematic trends that underscore the dominant role of nuclear shell effects in determining favored cluster emissions. Our calculations provide a comprehensive data set on the decay properties of superheavy isotopes for $Z = 107$ and $Z = 108$ and mass region $A = 267$–274, offering valuable insights into their stability and the underlying mechanisms of cluster radioactivity.

KEYWORDS
Deforming
Dluster
Driving potential
Binary decay
Half-live
Super heavy element

HISTORY
Received:
Revised:
Accepted:
Published:

1 Introduction

The first insights into the structure of the atomic nucleus were obtained at the beginning of the twentieth century through the study of radioactivity, following the pioneering discovery by Becquerel. For a long period, nuclear decay phenomena were believed to be limited to only three fundamental modes, namely α decay, β decay, and γ emission. This conventional picture of nuclear disintegration prevailed until theoretical advances suggested the possibility of more exotic decay channels.

In 1980, Sandulescu, Poenaru, and Greiner theoretically predicted the existence of a new type of nuclear decay lying intermediate between α decay and spontaneous fission, based on macroscopicmicroscopic considerations (Sandulescu et al., 1980). This decay mode, later termed cluster radioactivity, was experimentally confirmed in 1984 when Rose and Jones observed the emission of a ^{14}C nucleus from ^{223}Ra for the first time (Rose and Jones, 1984). This groundbreaking discovery opened a new field in nuclear physics and established cluster emission as a genuine decay mode of heavy nuclei.

Subsequent experimental and theoretical investigations revealed the emission of various clusters from different parent nuclei, particularly in the trans-lead and heavier regions of the nuclear chart. To date, the emission of clusters ranging from ^{14}C up to ^{34}Si and even heavier fragments has been confirmed for several parent nuclei. These observations demonstrated that cluster radioactivity is not an isolated phenomenon but a systematic decay process governed by nuclear structure effects (Gales et al., 1984; Poenaru and Greiner, 2010a,b; Poenaru et al., 2012).

From a theoretical standpoint, cluster radioactivity is analogous to α decay and is described as a quantum tunneling process. In order to be emitted, the preformed

*Corresponding author: m.azizi03@umail.umz.ac.ir

https://doi.org/

cluster must penetrate a potential barrier generated by the interplay of Coulomb, nuclear, and centrifugal interactions. One of the primary objectives in this domain is the accurate calculation of cluster decay half-lives. For computational simplicity, many models assume spherical shapes for the daughter and cluster nuclei, or consider axial quadrupole or ellipsoidal deformations for one of the fragments. A widely used and successful approach for half-life calculations is the one-dimensional WKB approximation, in which the decay probability is highly sensitive to the height and width of the effective potential barrier (Soylu et al., 2012; Pahlavani and Shamami, 2020).

The effective interaction potential plays a crucial role in determining decay half-lives. It is generally constructed as a sum of the Coulomb, nuclear, and centrifugal potentials. By employing suitable nuclear interaction potentials and incorporating additional physical effects such as nuclear deformation, temperature dependence, and shell corrections, the predictive power of half-life calculations can be significantly improved. These refinements have enabled systematic studies of cluster decay and fission-related processes in heavy and superheavy nuclei (Santhosh and Joseph, 2004; Zhang et al., 2016; Wei and Zhang, 2020).

Beyond conventional binary fission, heavy nuclei may also undergo more complex decay processes. Under certain conditions, the parent nucleus can split into three fragments simultaneously, giving rise to ternary fission. In this decay mode, two heavy fragments are accompanied by the emission of a lighter cluster, which may be emitted in equatorial or collinear geometrical configurations. Ternary fission can be regarded as a natural extension of binary fission and cluster radioactivity, reflecting the collective dynamics of highly deformed nuclear systems. Recent theoretical studies have demonstrated that cluster-accompanied ternary fission is energetically feasible for specific actinide nuclei and fragment combinations, with shell effects and fragment geometry playing a decisive role (Warda et al., 2018).

In this context, systematic investigations of ternary fission in heavy nuclei such as ^{248}Cf and ^{244}Fm have provided valuable insights into the influence of fragment mass asymmetry, nuclear deformation, and emission geometry on decay characteristics. Detailed comparisons between equatorial and collinear configurations, as well as analyses of light and heavy isobaric fragment combinations, have highlighted the importance of nuclear structure effects in determining the most probable ternary fission pathways (Pahlavani and Babi, 2024, 2025; Pahlavani and Saeidi Babi, 2025; Pahlavani and Saeidibabi, 2025). These studies emphasize that ternary fission represents a rich and complementary decay mode that bridges cluster radioactivity and spontaneous fission, offering a deeper understanding of multi-fragment decay mechanisms in heavy and superheavy nuclei.

Motivated by the ongoing interest in exotic decay modes and the need for reliable theoretical predictions in the superheavy mass region, the present work focuses on the calculation of cluster decay half-lives for superheavy parent nuclei with proton numbers $Z = 107$–108 and mass numbers $A = 267$–274. These nuclei lie in a region where strong Coulomb repulsion, shell effects, and deformation play a decisive role in determining decay characteristics. Within this framework, cluster emission is treated as a quantum tunneling process, and the decay half-lives are evaluated using a one-dimensional WKB approximation combined with an effective interaction potential consisting of Coulomb, nuclear, and centrifugal terms. By systematically investigating different clusterdaughter combinations, the present study aims to elucidate the role of nuclear structure effects on the stability and decay properties of superheavy nuclei.

The present study considers a representative set of emitted clusters, namely ^{6}He, ^{14}C, ^{18,20}O, ^{23}F, ^{22,24,25,26}Ne, ^{28,29,30}Mg, and ^{32,34}Si. These clusters were selected from the energetically allowed decay channels ($Q > 0$) to provide a systematic investigation of cluster radioactivity over a broad range of cluster masses. This representative set enables the study of the dependence of cluster decay properties on the emitted cluster mass and the associated nuclear structure effects in the superheavy region.

The organization of the paper is as follows. In Sec. 2, the theoretical framework and computational methodology employed for the calculation of cluster decay half-lives are presented, including the formulation of the interaction potential and the WKB penetration probability. Section 3 is devoted to the presentation and discussion of the numerical results, where the calculated half-lives are analyzed in relation to cluster mass, decay Q-values, and shell effects of the daughter nuclei. Finally, the main conclusions of the present study are summarized in Sec. 4.

2 Theoretical methods of calculations

Binary cluster decay is treated as a two–body quantum tunneling process in which the parent nucleus (Z_p, A_p) decays into a daughter nucleus (Z_d, A_d) and a preformed cluster (Z_c, A_c). Here, Z and A denote the proton (atomic) number and mass number, respectively, while the subscripts p, d, and c refer to the parent nucleus, daughter nucleus, and emitted cluster. The decay is governed by the total interaction potential and the tunneling probability obtained using the WKB approximation.

2.1 Q-value

The decay energy is

$$Q = M_p - (M_d + M_c), \tag{1}$$

where only channels with $Q > 0$ are considered. The quantity Q represents the energy released during the decay process, while M_p, M_d, and M_c are the mass excesses of the parent nucleus, daughter nucleus, and emitted cluster, respectively. The mass excess values were taken from the AME2020 atomic mass evaluation (Wang et al., 2021).

2.2 Total Interaction Potential

In this work, the total potential is

$$V(r) = V_C(r) + U_{AW}(r) + V_l(r), \tag{2}$$

where $V(r)$ is the total interaction potential between the daughter nucleus and the emitted cluster as a function of the center-to-center separation distance r. V_C is the Coulomb interaction, U_{AW} is the full Akyüz–Winther nuclear potential (Akyuz and Winther, 1979), and V_l is the centrifugal term.

2.2.1 Coulomb Potential

$$V_C(r) = \frac{Z_d Z_c e^2}{r}. \tag{3}$$

Here, Z_d and Z_c denote the atomic numbers of the daughter nucleus and emitted cluster, respectively, e is the elementary electric charge, and r is the separation distance between the centers of the two fragments.

2.3 Full Akyz–Winther Nuclear Potential

The Akyüz–Winther (AW) potential is used in its full microscopic–macroscopic form. The nuclear interaction is expressed as

$$U_{AW}(r) = -\frac{V_0}{1 + \exp\left(\dfrac{r - R_d - R_c}{a_v}\right)}, \tag{4}$$

where V_0 is the nuclear potential strength, R_d and R_c are the effective nuclear radii of the daughter nucleus and emitted cluster, respectively, and a_v is the diffuseness parameter describing the surface thickness of the nuclear potential.

2.3.1 Nuclear Strength Parameter

$$V_0 = 16\pi\gamma a_v \bar{R}, \tag{5}$$

with

$$\bar{R} = \frac{R_d R_c}{R_d + R_c}. \tag{6}$$

In these expressions, γ is the surface energy coefficient and $\bar{R}$ is the reduced radius characterizing the geometry of the interacting nuclei.

2.3.2 Nuclear Radii

The radii of interacting nuclei are given by

$$R_x = 1.20 A_x^{1/3} - 0.09 \text{ fm}, \qquad (x = d, c). \tag{7}$$

Here, A_x denotes the mass number of nucleus x, where $x = d$ corresponds to the daughter nucleus and $x = c$ to the emitted cluster.

2.3.3 Surface Tension Coefficient

The surface energy coefficient is

$$\gamma = 0.95\left(1 - 1.8\frac{N_d - Z_d}{A_d}\frac{N_c - Z_c}{A_c}\right). \tag{8}$$

The quantities N_d and N_c represent the neutron numbers of the daughter nucleus and emitted cluster, respectively.

2.3.4 Diffuseness Parameter

The diffuseness of the AW potential is (Akyuz and Winther, 1979)

$$a_v = \frac{1}{1.17\left(1 + 0.53 A_d^{-1/3} + A_c^{-1/3}\right)} \text{ fm}. \tag{9}$$

2.4 Centrifugal Potential

Angular momentum conservation leads to the centrifugal contribution (Langer, 1937)

$$V_l(r) = \frac{\hbar^2 l(l+1)}{2\mu r^2}, \tag{10}$$

with the reduced mass

$$\mu = m\frac{A_d A_c}{A_d + A_c}. \tag{11}$$

Here, l is the orbital angular momentum carried by the emitted cluster, μ is the reduced mass of the daughter–cluster system, $\hbar$ is the reduced Planck constant, and m denotes the nucleon mass.

The angular momentum l is fixed by spin–parity selection rules:

$$l = \begin{cases} \Delta_j, & \Delta_j \text{ even and } \pi_p = \pi_d, \\ \Delta_j + 1, & \Delta_j \text{ even and } \pi_p \neq \pi_d, \\ \Delta_j, & \Delta_j \text{ odd and } \pi_p \neq \pi_d, \\ \Delta_j + 1, & \Delta_j \text{ odd and } \pi_p = \pi_d, \end{cases} \tag{12}$$

where

$$\Delta_j = |j_p - j_d - j_c|. \tag{13}$$

In the above equations, j_p, j_d, and j_c denote the intrinsic spins of the parent nucleus, daughter nucleus, and emitted cluster, respectively, whereas π_p and π_d represent the corresponding parities.

2.5 Penetration Probability

The WKB transmission probability is

$$P = \exp\left[-\frac{2}{\hbar}\int_{r_{\text{in}}}^{r_{\text{out}}} \sqrt{2\mu\,(V(r) - Q)}\,dr\right], \tag{14}$$

where P is the barrier penetrability, while r_{in} and r_{out} are the inner and outer classical turning points determined from the condition $V(r) = Q$.

2.6 Decay Constant and Half-life

The half-life of cluster decay is evaluated as follows:

$$T_{1/2} = \frac{\ln 2}{\lambda}, \qquad \lambda = \nu P, \tag{15}$$

where λ is the decay constant, which represents the probability of decay per unit time, and ν is the assault frequency, i.e., the average number of barrier assaults made by the preformed cluster per second.

The assault frequency is obtained from

$$\nu = \frac{\omega}{2\pi} = \frac{2E_\nu}{h}, \tag{16}$$

where ω is the angular vibration frequency of the preformed cluster, E_ν is the empirical vibrational energy, and h is Planck's constant.

The vibrational energy is then calculated as

$$E_\nu = Q\left[0.056 + 0.039\exp\left(\frac{4 - A_{\mathrm{LCP}}}{2.5}\right)\right]\ \mathrm{MeV}, \tag{17}$$

where A_{LCP} denotes the mass number of the emitted light charged particle (cluster).

2.7 Computational Details

All numerical calculations presented in this work were performed using independent computational routines developed by the authors. The numerical implementation was carried out using Python, MATLAB, and Mathematica, allowing independent verification of the calculated interaction potentials, WKB barrier penetrabilities, decay constants, and half-lives. No previously published cluster-decay computational codes were employed in the present calculations. The Akyüz–Winther nuclear potential and all associated model parameters, including the nuclear radius, surface energy coefficient, and diffuseness parameter, were adopted directly from the original literature (Akyuz and Winther, 1979) without any modification, optimization, or iterative fitting procedure. Likewise, the remaining physical quantities, including the atomic mass excesses, were taken from the corresponding literature sources (Wang et al., 2021). Consequently, the calculated results represent direct predictions of the adopted theoretical model without the introduction of any adjustable parameters.

3 Results and Discussion

In this study, we systematically analyzed the cluster radioactivity of superheavy nuclei ^{267,270,271,272,274}Bh ($Z = 107$) and ^{268,269,270,271,272}Hs ($Z = 108$). Using a binary decay model, we computed Q-values, interaction barriers, driving potentials ($V - Q$), penetrabilities, decay constants, and half-lives for multiple clusters: ^{6}He, ^{14}C, ^{18,20}O, ^{23}F, ^{22,24,25,26}Ne, ^{28,29,30}Mg, and ^{32,34}Si. All results are presented in Tables 1–10 and Figs. 1–2.

3.1 Bohrium Isotopes ($Z = 107$)

^{267}Bh. The cluster decay landscape of ^{267}Bh is shaped by pronounced nuclear shell effects, with silicon emissions demonstrating clear dominance. The ^{32}Si cluster ($Z = 14$, $N = 18$) emerges as the optimal decay pathway, achieving the highest Q-value of 101.80 MeV when forming the daughter ^{235}Am ($Z = 95$, $N = 140$) and exhibiting the maximum penetrability of $P = 1.72 \times 10^{-37}$. These conditions yield the shortest half-life of $T_{1/2} = 1.46 \times 10^{15}$ s. In contrast, the even magic ^{34}Si ($Z = 14$, $N = 20$) presents a competitive $Q = 100.80$ MeV but experiences a significantly reduced penetrability of $P = 5.53 \times 10^{-39}$, illustrating how structural properties beyond simple energetics govern tunneling dynamics. Figure 1-a captures this nuanced competition, while Table 1 documents the complete dataset, including mid-mass clusters such as ^{24}Ne ($Z = 10$, $N = 14$) with $T_{1/2} = 3.88 \times 10^{17}$ s.

^{270}Bh. For ^{270}Bh, silicon emissions maintain prominence with distinctive quantitative characteristics. The ^{32}Si cluster ($Z = 14$, $N = 18$) delivers the highest $Q = 100.85$ MeV and shortest half-life of $T_{1/2} = 9.47 \times 10^{15}$ s, corresponding to the daughter ^{238}Pu ($Z = 94$). Despite a nearly identical Q-value of 100.84 MeV, ^{34}Si ($Z = 14$, $N = 20$) shows a penetrability of $P = 1.10 \times 10^{-38}$ that is approximately 2.4 times lower than ^{32}Si's $P = 2.68 \times 10^{-38}$, suggesting subtle structural influences on barrier penetration. Figure 1-b reveals an additional penetrability peak for ^{28}Mg ($Z = 12$, $N = 16$, $P = 2.24 \times 10^{-40}$), while the ^{20}O cluster ($Z = 8$, $N = 12$) displays the shallowest potential minimum of 26.73 MeV. All calculated values are compiled in Table 2.

^{271}Bh. In the odd-neutron nucleus ^{271}Bh ($N = 164$), silicon isotopes exhibit a balanced competition. ^{34}Si ($Z = 14$, $N = 20$) attains the highest $Q = 100.98$ MeV, while its counterpart ^{32}Si ($Z = 14$, $N = 18$) follows closely with $Q = 100.62$ MeV. Their comparable penetrabilities$P = 1.93 \times 10^{-38}$ and $P = 1.81 \times 10^{-38}$, respectivelyresult in similar half-lives: $T_{1/2} = 1.31 \times 10^{16}$ s for ^{34}Si and $T_{1/2} = 1.41 \times 10^{16}$ s for ^{32}Si. The ^{20}O cluster ($Z = 8$, $N = 12$) shows the shallowest potential minimum at $V = 26.28$ MeV, corresponding to an assault frequency $\nu = 1.29 \times 10^{21}$ Hz. At the opposite extreme, ^{23}F ($Z = 9$, $N = 14$) exhibits minimal penetrability of $P = 1.48 \times 10^{-48}$. The full penetrability spectrum appears in Fig. 1-c, with detailed results in Table 3.

^{272}Bh. The decay characteristics of ^{272}Bh further emphasize silicon dominance with quantitative refinements. ^{34}Si ($Z = 14$, $N = 20$) yields the highest $Q = 101.32$ MeV, the greatest penetrability of $P = 5.82 \times 10^{-38}$, and the shortest half-life of $T_{1/2} = 4.34 \times 10^{15}$ s. The near-magic ^{32}Si ($Z = 14$, $N = 18$) presents $Q = 100.55$ MeV and $T_{1/2} = 1.43 \times 10^{16}$ s. Beyond silicon, ^{28}Mg ($Z = 12$, $N = 16$) emerges as a notable mid-mass candidate with $Q = 83.93$ MeV and $T_{1/2} = 6.29 \times 10^{17}$ s, while lighter clusters such as ^{22}Ne experience suppression exceeding fifteen orders of magnitude in half-life. These trends are visualized in Fig. 1-d and quantified in Table 4.

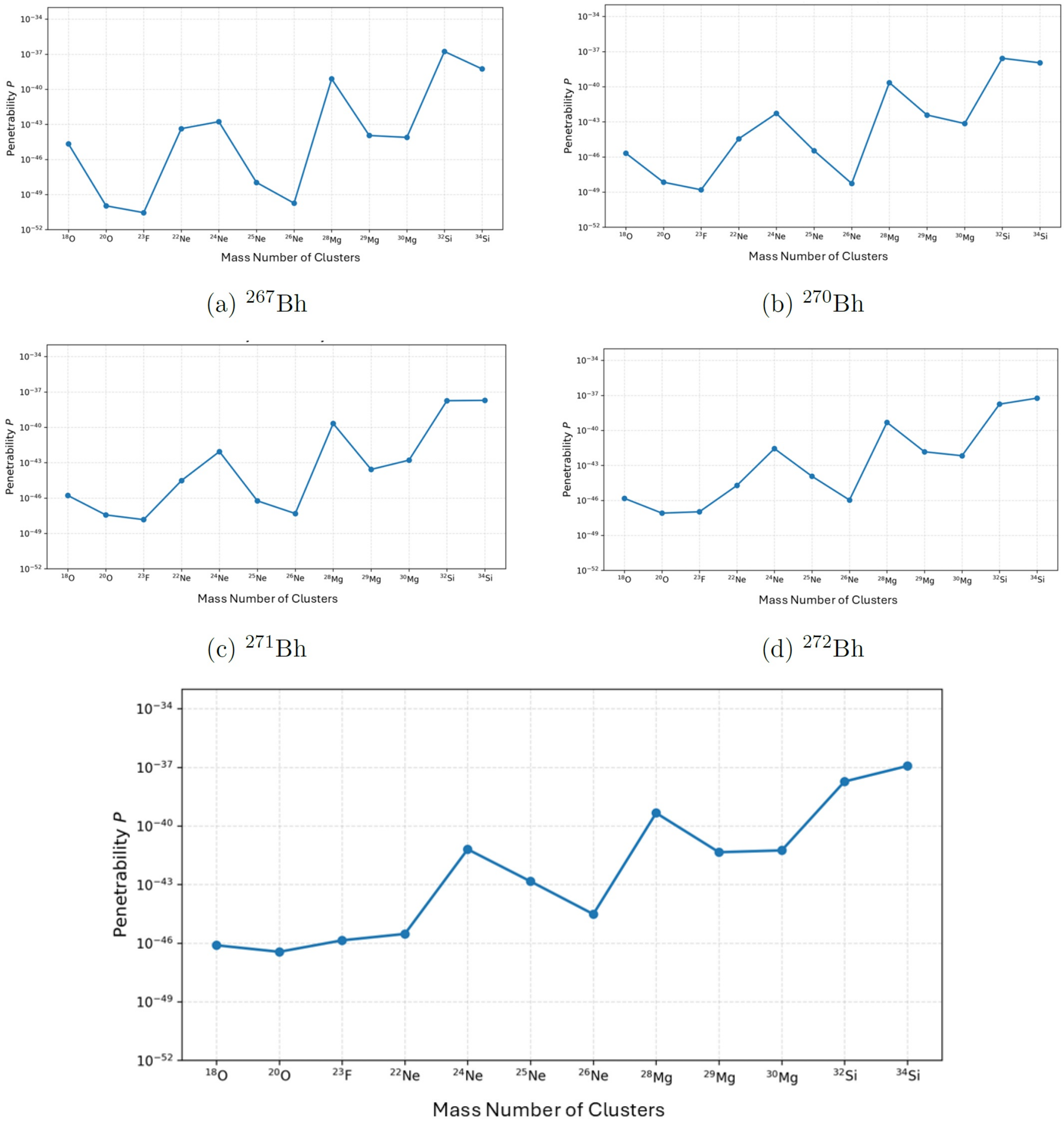

(a) ^{267}Bh

(b) ^{270}Bh

(c) ^{271}Bh

(d) ^{272}Bh

(e) ^{274}Bh

Figure 1: enetration probability as a function of emitted cluster mass number for the five berkelium isotopes: (a) ^{267}Bh, (b) ^{270}Bh, (c) ^{271}Bh, (d) ^{272}Bh, and (e) ^{274}Bh. The plots illustrate the systematic variation in tunneling probabilities across different cluster emissions, with peaks indicating the most probable decay channels for each isotope.

^{274}Bh. In neutron-rich ^{274}Bh ($N = 167$), heavy cluster emission is strongly enhanced. ^{34}Si ($Z = 14$, $N = 20$) dominates with the highest $Q = 101.44$ MeV, maximum penetrability of $P = 1.17 \times 10^{-37}$, and shortest half-life of $T_{1/2} = 2.16 \times 10^{15}$ s. The near-magic ^{32}Si ($Z = 14$, $N = 18$) follows with $Q = 100.42$ MeV and $T_{1/2} = 1.36 \times 10^{16}$ s. Mid-mass ^{28}Mg ($Z = 12$, $N = 16$) maintains relevance with $T_{1/2} = 6.65 \times 10^{17}$ s, while ^{24}Ne ($Z = 10$, $N = 14$) marks the transition to light clusters with $T_{1/2} = 6.03 \times 10^{19}$ s. The systematic half-life increase with decreasing cluster mass underscores the interplay between Q-value and Coulomb barrier. Figure 1-e and Table 5 provide comprehensive visualization and data.

3.2 *Hassium Isotopes* ($Z = 108$)

^{268}Hs. The cluster decay of ^{268}Hs is dominated by silicon emissions, with ^{32}Si ($Z = 14$, $N = 18$) exhibiting the highest Q-value of 104.14 MeV and the shortest half-life of $T_{1/2} = 8.27 \times 10^{13}$ s. Its penetrability of $P = 2.97 \times 10^{-36}$ is the largest among all considered clusters. The doubly magic ^{34}Si ($Z = 14$, $N = 20$) follows with $Q = 102.61$

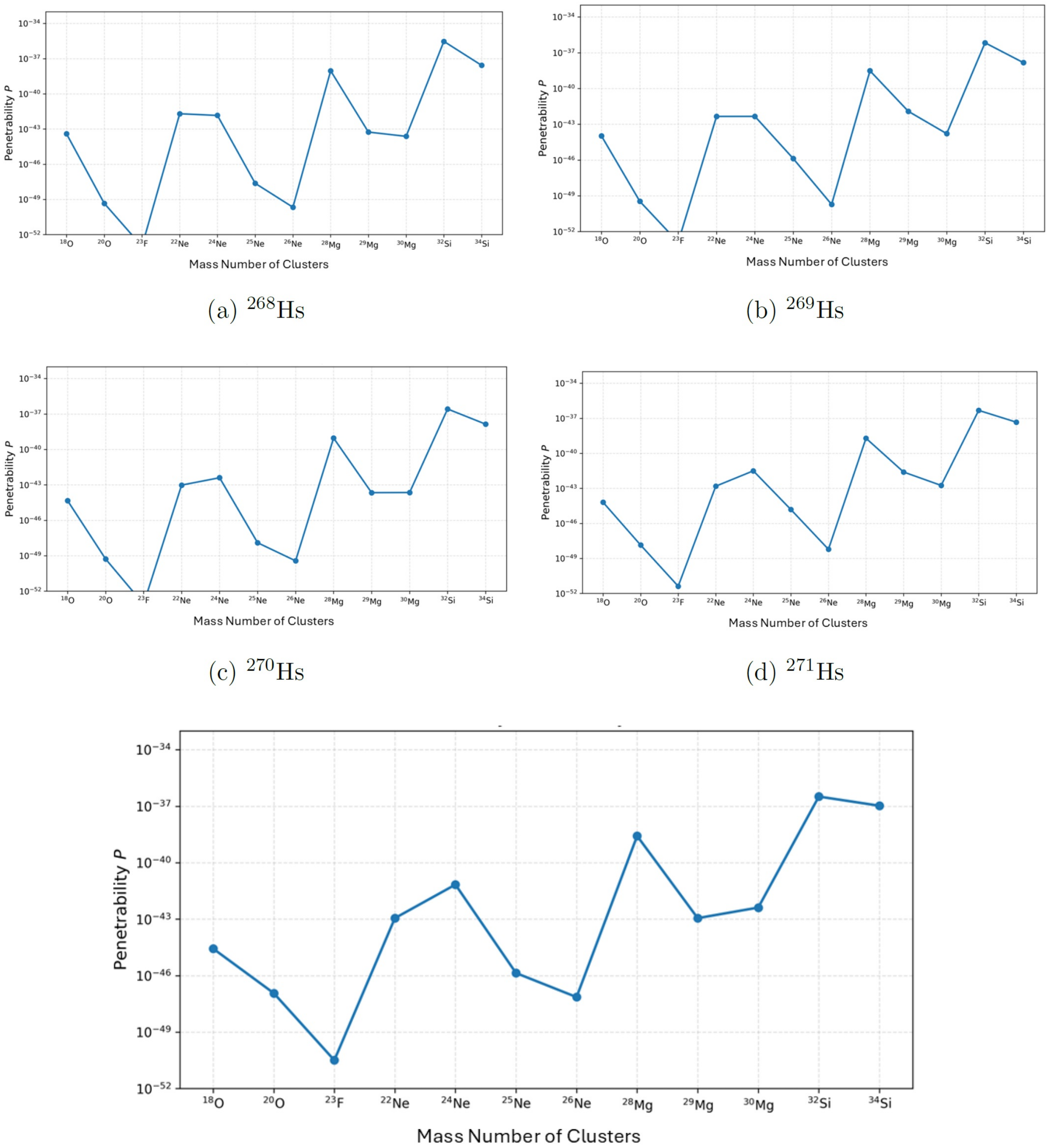

(a) ^{268}Hs (b) ^{269}Hs (c) ^{270}Hs (d) ^{271}Hs (e) ^{272}Hs

Figure 2: Penetration probability as a function of emitted cluster mass number for the five hassium isotopes: (a) ^{268}Hs, (b) ^{269}Hs, (c) ^{270}Hs, (d) ^{271}Hs, and (e) ^{272}Hs. The plots demonstrate the variation in tunneling probabilities across different cluster emissions for $Z = 108$ nuclei, highlighting the most favorable decay channels for each isotope.

MeV and $T_{1/2} = 9.27 \times 10^{15}$ s. Beyond silicon, ^{28}Mg ($Z = 12$, $N = 16$) presents a competitive half-life of $T_{1/2} = 3.21 \times 10^{16}$ s, while ^{22}Ne ($Z = 10$, $N = 12$) is suppressed by several orders of magnitude. The full penetrability spectrum is shown in Fig. 2-a, and detailed results are compiled in Table 6.

^{269}**Hs.** For ^{269}Hs, ^{32}Si again dominates with $Q = 103.48$ MeV and $T_{1/2} = 3.63 \times 10^{14}$ s, accompanied by a penetrability of $P = 6.82 \times 10^{-37}$. The ^{34}Si cluster yields $Q = 102.30$ MeV and $T_{1/2} = 1.70 \times 10^{16}$ s. The ^{28}Mg isotope remains a notable mid-mass candidate with $T_{1/2} = 9.78 \times 10^{16}$ s, while the odd-neutron ^{29}Mg exhibits a longer half-life of $T_{1/2} = 2.52 \times 10^{20}$ s. These trends are visualized in Fig. 2-b and tabulated in Table 7.

^{270}**Hs.** In ^{270}Hs, the ^{32}Si cluster maintains its leading role with $Q = 103.03$ MeV and $T_{1/2} = 9.37 \times 10^{14}$ s, while ^{34}Si follows with $Q = 102.20$ MeV and $T_{1/2} = 1.81 \times 10^{16}$ s. The ^{28}Mg emission shows a half-life of $T_{1/2} = 3.27 \times 10^{17}$ s, and the neutron-rich ^{30}Mg is highly suppressed with $T_{1/2} = 1.39 \times 10^{22}$ s. The penetrability distribution across clusters is displayed in Fig. 2-c, with complete data available in Table 8.

^{271}Hs. The decay spectrum of ^{271}Hs is characterized by ^{32}Si emission, which yields $Q = 103.18$ MeV and $T_{1/2} = 5.21 \times 10^{14}$ s. The ^{34}Si cluster presents $Q = 102.59$ MeV and $T_{1/2} = 5.34 \times 10^{15}$ s. Mid-mass clusters such as ^{28}Mg and ^{24}Ne exhibit half-lives of $T_{1/2} = 1.53 \times 10^{17}$ s and $T_{1/2} = 1.20 \times 10^{20}$ s, respectively. Figure 2-d illustrates the corresponding penetrability trends, and Table 9 provides the full dataset.

^{272}Hs. For the neutron-rich ^{272}Hs, ^{32}Si remains the most favorable cluster with $Q = 102.96$ MeV and $T_{1/2} = 7.65 \times 10^{14}$ s. Interestingly, ^{34}Si shows a significantly enhanced penetrability of $P = 1.06 \times 10^{-37}$ and a half-life of $T_{1/2} = 2.35 \times 10^{15}$ s. The ^{28}Mg and ^{24}Ne clusters display half-lives of $T_{1/2} = 1.14 \times 10^{17}$ s and $T_{1/2} = 5.53 \times 10^{19}$ s, respectively. The systematic variation in penetrability with cluster mass is captured in Fig. 2-e, and all calculated values are compiled in Table 10.

3.3 Comparative Analysis and Nuclear Structure Effects

The comprehensive analysis of cluster decay across Bohrium and Hassium isotopes reveals fundamental nuclear structure effects that govern decay preferences and probabilities. Figure 3 presents the collective penetration probability distributions, with panel (a) showing Bh isotopes and panel (b) showing Hs isotopes. The consistent dominance of silicon clusters (^{32}Si and ^{34}Si) across both series is particularly striking, with pronounced peaks at $A_c \approx 32 - 34$. This preference emerges from the combined shell effects in both the emitted cluster and the residual daughter nucleus. The even-magic ^{34}Si ($Z = 14$, $N = 20$) exhibits enhanced stability due to shell closures, while ^{32}Si ($Z = 14$, $N = 18$), being near the $N = 20$ shell closure, benefits from similar structural advantages. The resulting daughter nuclei following silicon emission approach shell-stabilized configurations, particularly evident in decays leading to ^{238}Pu ($Z = 94$, $N = 144$) and other nuclei near the $N = 144$ subshell closure.

The secondary maxima observed for magnesium clusters ($^{28-30}$Mg) in Fig. 3 demonstrate how mid-mass clusters can compete when they connect parent and daughter nuclei to favorable shell structures. For instance, ^{28}Mg emission often leads to daughters near the $Z = 94 - 96$, $N = 144 - 146$ region, which experience enhanced stability. The systematic suppression of light clusters (Ne, O, F) reflects the diminishing influence of shell effects as cluster size decreases, making these emissions increasingly dependent on pure energetics rather than structural stabilization.

Figure 4 displays the Geiger-Nuttall relationships, plotting $\log_{10}(T_{1/2})$ against the parameter $Z_d Z_c/\sqrt{Q}$, where Z_d and Z_c are the atomic numbers of daughter and cluster, respectively. Panel (a) for Bh isotopes and panel (b) for Hs isotopes both reveal cluster-specific linear correlations, but with notable nuclear structure effects manifesting as deviations from perfect linearity. Silicon clusters form the lowest-lying lines, indicating their structural preference beyond what the simple Coulomb-energy parameter would predict. The systematic offset between ^{32}Si and ^{34}Si trends, despite their similar $Z_d Z_c/\sqrt{Q}$ values, directly illustrates how shell closures in the cluster itself modify tunneling probabilities. This effect is particularly pronounced in Hs isotopes, where the $N = 162$ subshell closure in the parent nuclei influences the decay energetics of different cluster types.

The influence of odd-even effects is observable throughout both isotopic series. In odd-neutron nuclei like ^{271}Bh ($N = 164$) and ^{269}Hs ($N = 161$), certain clusters exhibit slightly enhanced or suppressed probabilities compared to their even-even neighbors. This suggests that the single unpaired neutron can modify the preformation probability of specific clusters, likely through its influence on nuclear pairing correlations and collective degrees of freedom.

The combined analysis highlights several key nuclear structure findings:

- **Dual shell effects**: The most probable emissions occur when both the emitted cluster and the residual daughter nucleus approach magic or near-magic configurations, maximizing the energy release and minimizing the potential barrier.
- **Structural hierarchy**: Clusters can be ranked by their structural favorability: silicon (magic or near-magic) ¿ magnesium (transitional shell region) ¿ neon/oxygen (weak shell effects).
- **Neutron number systematics**: Increasing neutron number enhances the probability of heavy cluster emission while suppressing light clusters, as the neutron-rich environment stabilizes heavier fragmentation patterns.
- **Geiger-Nuttall deviations**: The linear correlations in Fig. 4 show systematic offsets between different cluster types that correlate with their shell structure, providing a quantitative measure of nuclear structure effects beyond the simple tunneling model.

To place the present calculations in context, we note that systematic theoretical investigations of cluster radioactivity have mainly focused on heavier superheavy nuclei ($Z \geq 116$), while corresponding studies for Bh ($Z = 107$) and Hs ($Z = 108$) isotopes remain very limited. Previous theoretical works have shown that cluster decay in the superheavy region is strongly governed by the decay energy and nuclear shell effects, with favored decay channels corresponding to enhanced stability of the resulting fragments (Santhosh and Priyanka, 2014; Liu et al., 2024). The systematic trends obtained in the present work, including the increase in penetrability with increasing Q-value and the preference for specific silicon-cluster emissions, are consistent with these general theoretical expectations, while extending such investigations to the previously unexplored Bh and Hs isotopic chains.

These findings collectively demonstrate that cluster radioactivity in superheavy nuclei is not merely a quantum tunneling phenomenon but a sensitive probe of nuclear

Table 1: Cluster decay properties for parent nucleus ^{267}Bh.

Daughter	Cluster	Q (MeV)	P	V (MeV)	ν (s^{-1})	$T_{1/2}$ (s)
^{249}Es	^{18}O	48.37	2.14×10^{-45}	27.80	1.31×10^{21}	2.47×10^{23}
^{247}Es	^{20}O	46.39	1.09×10^{-50}	27.91	1.26×10^{21}	5.06×10^{28}
^{244}Cf	^{23}F	54.00	2.83×10^{-51}	29.91	1.46×10^{21}	1.67×10^{29}
^{245}Bk	^{22}Ne	64.98	4.31×10^{-44}	31.64	1.76×10^{21}	9.13×10^{21}
^{243}Bk	^{24}Ne	66.03	1.71×10^{-43}	28.87	1.79×10^{21}	2.27×10^{21}
^{242}Bk	^{25}Ne	63.05	1.09×10^{-48}	31.04	1.71×10^{21}	3.72×10^{26}
^{241}Bk	^{26}Ne	62.30	1.83×10^{-50}	31.01	1.69×10^{21}	2.24×10^{28}
^{239}Am	^{28}Mg	84.39	7.81×10^{-40}	29.91	2.29×10^{21}	3.88×10^{17}
^{238}Am	^{29}Mg	80.96	1.12×10^{-44}	32.59	2.19×10^{21}	2.82×10^{22}
^{237}Am	^{30}Mg	81.08	7.74×10^{-45}	31.74	2.20×10^{21}	4.08×10^{22}
^{235}Np	^{32}Si	101.80	1.72×10^{-37}	30.78	2.76×10^{21}	1.46×10^{15}
^{233}Np	^{34}Si	100.81	5.53×10^{-39}	30.37	2.73×10^{21}	4.59×10^{16}

Table 2: Cluster decay properties for parent nucleus ^{270}Bh.

Daughter	Cluster	Q (MeV)	P	V (MeV)	ν (s^{-1})	$T_{1/2}$ (s)
^{252}Es	^{18}O	47.72	2.09×10^{-46}	28.10	1.30×10^{21}	2.56×10^{24}
^{250}Es	^{20}O	47.21	6.97×10^{-49}	26.74	1.28×10^{21}	7.77×10^{26}
^{247}Cf	^{23}F	54.84	1.57×10^{-49}	28.69	1.49×10^{21}	2.97×10^{27}
^{248}Bk	^{22}Ne	64.12	3.57×10^{-45}	32.08	1.74×10^{21}	1.12×10^{23}
^{246}Bk	^{24}Ne	66.21	5.23×10^{-43}	28.26	1.79×10^{21}	7.39×10^{20}
^{245}Bk	^{25}Ne	64.45	3.45×10^{-46}	29.22	1.75×10^{21}	1.15×10^{24}
^{244}Bk	^{26}Ne	63.04	5.38×10^{-49}	29.86	1.71×10^{21}	7.55×10^{26}
^{242}Am	^{28}Mg	83.78	2.24×10^{-40}	30.05	2.27×10^{21}	1.36×10^{18}
^{241}Am	^{29}Mg	81.91	3.85×10^{-43}	31.16	2.22×10^{21}	8.12×10^{20}
^{240}Am	^{30}Mg	81.60	7.15×10^{-44}	30.74	2.21×10^{21}	4.39×10^{21}
^{238}Np	^{32}Si	100.85	2.68×10^{-38}	31.19	2.73×10^{21}	9.47×10^{15}
^{236}Np	^{34}Si	100.84	1.10×10^{-38}	29.80	2.73×10^{21}	2.31×10^{16}

Table 3: Cluster decay properties for parent nucleus ^{271}Bh.

Daughter	Cluster	Q (MeV)	P	V (MeV)	ν (s^{-1})	$T_{1/2}$ (s)
^{253}Es	^{18}O	47.63	1.66×10^{-46}	28.07	1.29×10^{21}	3.23×10^{24}
^{251}Es	^{20}O	47.55	3.73×10^{-48}	26.28	1.29×10^{21}	1.44×10^{26}
^{248}Cf	^{23}F	55.34	1.48×10^{-48}	28.06	1.50×10^{21}	3.12×10^{26}
^{249}Bk	^{22}Ne	64.04	3.08×10^{-45}	32.03	1.74×10^{21}	1.30×10^{23}
^{247}Bk	^{24}Ne	66.32	8.82×10^{-43}	28.02	1.80×10^{21}	4.37×10^{20}
^{246}Bk	^{25}Ne	63.93	5.83×10^{-47}	29.60	1.73×10^{21}	6.87×10^{24}
^{245}Bk	^{26}Ne	63.56	4.87×10^{-48}	29.19	1.72×10^{21}	8.27×10^{25}
^{243}Am	^{28}Mg	83.70	2.11×10^{-40}	29.96	2.27×10^{21}	1.45×10^{18}
^{242}Am	^{29}Mg	81.00	2.68×10^{-44}	31.91	2.19×10^{21}	1.18×10^{22}
^{241}Am	^{30}Mg	81.81	1.64×10^{-43}	30.38	2.22×10^{21}	1.91×10^{21}
^{239}Np	^{32}Si	100.63	1.81×10^{-38}	31.24	2.73×10^{21}	1.41×10^{16}
^{237}Np	^{34}Si	100.98	1.93×10^{-38}	29.48	2.73×10^{21}	1.31×10^{16}

Table 4: Cluster decay properties for parent nucleus ^{272}Bh.

Daughter	Cluster	Q (MeV)	P	V (MeV)	ν (s^{-1})	$T_{1/2}$ (s)
^{254}Es	^{18}O	47.58	1.50×10^{-46}	28.01	1.29×10^{21}	3.58×10^{24}
^{252}Es	^{20}O	47.70	8.13×10^{-48}	26.02	1.29×10^{21}	6.59×10^{25}
^{249}Cf	^{23}F	55.78	1.06×10^{-47}	27.49	1.51×10^{21}	4.33×10^{25}
^{250}Bk	^{22}Ne	63.86	1.91×10^{-45}	32.07	1.73×10^{21}	2.10×10^{23}
^{248}Bk	^{24}Ne	66.61	2.75×10^{-42}	27.59	1.80×10^{21}	1.40×10^{20}
^{247}Bk	^{25}Ne	65.33	1.17×10^{-44}	28.06	1.77×10^{21}	3.35×10^{22}
^{246}Bk	^{26}Ne	64.34	1.08×10^{-46}	28.28	1.74×10^{21}	3.68×10^{24}
^{244}Am	^{28}Mg	83.93	4.85×10^{-40}	29.58	2.27×10^{21}	6.29×10^{17}
^{243}Am	^{29}Mg	82.22	1.47×10^{-42}	30.53	2.23×10^{21}	2.12×10^{20}
^{242}Am	^{30}Mg	82.20	6.75×10^{-43}	29.82	2.23×10^{21}	4.61×10^{20}
^{240}Np	^{32}Si	100.55	1.78×10^{-38}	31.14	2.72×10^{21}	1.43×10^{16}
^{238}Np	^{34}Si	101.32	5.82×10^{-38}	28.96	2.74×10^{21}	4.34×10^{15}

Table 5: Cluster decay properties for parent nucleus ^{274}Bh.

Daughter	Cluster	Q (MeV)	P	V (MeV)	ν (s^{-1})	$T_{1/2}$ (s)
^{256}Es	^{18}O	47.36	7.77×10^{-47}	27.99	1.29×10^{21}	6.94×10^{24}
^{254}Es	^{20}O	47.97	3.60×10^{-47}	25.51	1.30×10^{21}	1.48×10^{25}
^{251}Cf	^{23}F	56.34	1.39×10^{-46}	26.68	1.53×10^{21}	3.27×10^{24}
^{252}Bk	^{22}Ne	63.25	2.97×10^{-46}	32.40	1.71×10^{21}	1.36×10^{24}
^{250}Bk	^{24}Ne	66.76	6.36×10^{-42}	27.17	1.81×10^{21}	6.03×10^{19}
^{249}Bk	^{25}Ne	65.95	1.45×10^{-43}	27.17	1.79×10^{21}	2.68×10^{21}
^{248}Bk	^{26}Ne	65.15	3.04×10^{-45}	27.20	1.76×10^{21}	1.29×10^{23}
^{246}Am	^{28}Mg	83.79	4.59×10^{-40}	29.41	2.27×10^{21}	6.65×10^{17}
^{245}Am	^{29}Mg	82.47	4.51×10^{-42}	29.97	2.23×10^{21}	6.88×10^{19}
^{244}Am	^{30}Mg	82.76	5.59×10^{-42}	28.95	2.24×10^{21}	5.53×10^{19}
^{242}Np	^{32}Si	100.42	1.88×10^{-38}	30.91	2.72×10^{21}	1.36×10^{16}
^{240}Np	^{34}Si	101.44	1.17×10^{-37}	28.50	2.75×10^{21}	2.16×10^{15}

structure, where shell closures, pairing correlations, and shape degrees of freedom collectively determine the most

Table 6: Cluster decay properties for parent nucleus ^{268}Hs.

Daughter	Cluster	Q (MeV)	P	V (MeV)	ν (s^{-1})	$T_{1/2}$ (s)
^{250}Fm	^{18}O	49.68	3.90×10^{-44}	27.47	1.35×10^{21}	1.32×10^{22}
^{248}Fm	^{20}O	47.27	4.62×10^{-50}	27.99	1.28×10^{21}	1.17×10^{28}
^{245}Es	^{23}F	53.37	9.97×10^{-54}	31.62	1.45×10^{21}	4.81×10^{31}
^{246}Cf	^{22}Ne	66.90	2.01×10^{-42}	30.93	1.81×10^{21}	1.90×10^{20}
^{244}Cf	^{24}Ne	67.44	1.44×10^{-42}	28.65	1.83×10^{21}	2.63×10^{20}
^{243}Cf	^{25}Ne	64.01	2.35×10^{-48}	31.27	1.73×10^{21}	1.70×10^{26}
^{242}Cf	^{26}Ne	63.10	2.15×10^{-50}	31.40	1.71×10^{21}	1.89×10^{28}
^{240}Cm	^{28}Mg	86.26	9.24×10^{-39}	29.47	2.34×10^{21}	3.21×10^{16}
^{239}Cm	^{29}Mg	82.43	5.50×10^{-44}	32.53	2.23×10^{21}	5.65×10^{21}
^{238}Cm	^{30}Mg	82.40	2.38×10^{-44}	31.83	2.23×10^{21}	1.31×10^{22}
^{236}Pu	^{32}Si	104.14	2.97×10^{-36}	30.08	2.82×10^{21}	8.27×10^{13}
^{234}Pu	^{34}Si	102.61	2.69×10^{-38}	30.21	2.78×10^{21}	9.27×10^{15}

Table 7: Cluster decay properties for parent nucleus ^{269}Hs.

Daughter	Cluster	Q (MeV)	P	V (MeV)	ν (s^{-1})	$T_{1/2}$ (s)
^{251}Fm	^{18}O	49.32	1.05×10^{-44}	27.71	1.34×10^{21}	4.93×10^{22}
^{249}Fm	^{20}O	47.18	3.43×10^{-50}	27.97	1.28×10^{21}	1.58×10^{28}
^{246}Es	^{23}F	53.39	1.28×10^{-53}	31.47	1.45×10^{21}	3.74×10^{31}
^{247}Cf	^{22}Ne	66.41	4.55×10^{-43}	31.28	1.80×10^{21}	8.47×10^{20}
^{245}Cf	^{24}Ne	67.06	4.59×10^{-43}	28.89	1.82×10^{21}	8.31×10^{20}
^{244}Cf	^{25}Ne	65.05	1.32×10^{-46}	30.09	1.76×10^{21}	2.98×10^{24}
^{243}Cf	^{26}Ne	63.02	1.88×10^{-50}	31.34	1.71×10^{21}	2.16×10^{28}
^{241}Cm	^{28}Mg	85.81	3.05×10^{-39}	29.76	2.32×10^{21}	9.78×10^{16}
^{240}Cm	^{29}Mg	83.38	1.22×10^{-42}	31.42	2.26×10^{21}	2.52×10^{20}
^{239}Cm	^{30}Mg	82.23	1.63×10^{-44}	31.84	2.23×10^{21}	1.91×10^{22}
^{237}Pu	^{32}Si	103.48	6.82×10^{-37}	30.57	2.80×10^{21}	3.63×10^{14}
^{235}Pu	^{34}Si	102.30	1.47×10^{-38}	30.33	2.77×10^{21}	1.70×10^{16}

Table 8: Cluster decay properties for parent nucleus ^{270}Hs.

Daughter	Cluster	Q (MeV)	P	V (MeV)	ν (s^{-1})	$T_{1/2}$ (s)
^{252}Fm	^{18}O	49.08	4.57×10^{-45}	27.83	1.33×10^{21}	1.14×10^{23}
^{250}Fm	^{20}O	47.24	5.32×10^{-50}	27.79	1.28×10^{21}	1.02×10^{28}
^{247}Es	^{23}F	53.25	7.93×10^{-54}	31.48	1.44×10^{21}	6.06×10^{31}
^{248}Cf	^{22}Ne	65.90	9.55×10^{-44}	31.65	1.79×10^{21}	4.06×10^{21}
^{246}Cf	^{24}Ne	66.97	4.01×10^{-43}	28.84	1.81×10^{21}	9.53×10^{20}
^{245}Cf	^{25}Ne	63.76	1.26×10^{-48}	31.24	1.73×10^{21}	3.19×10^{26}
^{244}Cf	^{26}Ne	63.15	3.69×10^{-50}	31.07	1.71×10^{21}	1.10×10^{28}
^{242}Cm	^{28}Mg	85.33	9.17×10^{-40}	30.08	2.31×10^{21}	3.27×10^{17}
^{241}Cm	^{29}Mg	82.02	2.18×10^{-44}	32.62	2.22×10^{21}	1.43×10^{22}
^{240}Cm	^{30}Mg	82.27	2.24×10^{-44}	31.64	2.23×10^{21}	1.39×10^{22}
^{238}Pu	^{32}Si	103.03	2.65×10^{-37}	30.84	2.79×10^{21}	9.37×10^{14}
^{236}Pu	^{34}Si	102.20	1.38×10^{-38}	30.25	2.77×10^{21}	1.81×10^{16}

Table 9: Cluster decay properties for parent nucleus ^{271}Hs.

Daughter	Cluster	Q (MeV)	P	V (MeV)	ν (s^{-1})	$T_{1/2}$ (s)
^{253}Fm	^{18}O	49.13	6.38×10^{-45}	27.67	1.33×10^{21}	8.14×10^{22}
^{251}Fm	^{20}O	47.94	1.38×10^{-48}	26.98	1.30×10^{21}	3.86×10^{26}
^{248}Es	^{23}F	54.11	4.13×10^{-52}	30.50	1.47×10^{21}	1.14×10^{30}
^{249}Cf	^{22}Ne	65.99	1.53×10^{-43}	31.41	1.79×10^{21}	2.53×10^{21}
^{247}Cf	^{24}Ne	67.53	3.15×10^{-42}	28.14	1.83×10^{21}	1.20×10^{20}
^{246}Cf	^{25}Ne	65.64	1.53×10^{-45}	29.22	1.78×10^{21}	2.55×10^{23}
^{245}Cf	^{26}Ne	63.82	6.00×10^{-49}	30.26	1.73×10^{21}	6.68×10^{26}
^{243}Cm	^{28}Mg	85.53	1.95×10^{-39}	29.72	2.32×10^{21}	1.53×10^{17}
^{242}Cm	^{29}Mg	83.50	2.50×10^{-42}	30.99	2.26×10^{21}	1.23×10^{20}
^{241}Cm	^{30}Mg	82.87	1.78×10^{-43}	30.88	2.24×10^{21}	1.74×10^{21}
^{239}Pu	^{32}Si	103.18	4.76×10^{-37}	30.51	2.79×10^{21}	5.21×10^{14}
^{237}Pu	^{34}Si	102.59	4.67×10^{-38}	29.68	2.78×10^{21}	5.34×10^{15}

Table 10: Cluster decay properties for parent nucleus ^{272}Hs.

Daughter	Cluster	Q (MeV)	P	V (MeV)	ν (s^{-1})	$T_{1/2}$ (s)
^{254}Fm	^{18}O	48.88	2.70×10^{-45}	27.79	1.33×10^{21}	1.93×10^{23}
^{252}Fm	^{20}O	48.39	1.17×10^{-47}	26.41	1.31×10^{21}	4.52×10^{25}
^{249}Es	^{23}F	54.54	3.19×10^{-51}	29.93	1.48×10^{21}	1.47×10^{29}
^{250}Cf	^{22}Ne	65.86	1.13×10^{-43}	31.41	1.78×10^{21}	3.44×10^{21}
^{248}Cf	^{24}Ne	67.72	6.83×10^{-42}	27.82	1.83×10^{21}	5.53×10^{19}
^{247}Cf	^{25}Ne	64.93	1.37×10^{-46}	29.79	1.76×10^{21}	2.88×10^{24}
^{246}Cf	^{26}Ne	64.43	7.23×10^{-48}	29.51	1.75×10^{21}	5.49×10^{25}
^{244}Cm	^{28}Mg	85.57	2.63×10^{-39}	29.52	2.32×10^{21}	1.14×10^{17}
^{243}Cm	^{29}Mg	82.43	1.13×10^{-43}	31.89	2.23×10^{21}	2.75×10^{21}
^{242}Cm	^{30}Mg	83.08	4.13×10^{-43}	30.51	2.25×10^{21}	7.46×10^{20}
^{240}Pu	^{32}Si	102.96	3.25×10^{-37}	30.55	2.79×10^{21}	7.65×10^{14}
^{238}Pu	^{34}Si	102.83	1.06×10^{-37}	29.26	2.78×10^{21}	2.35×10^{15}

probable decay pathways.

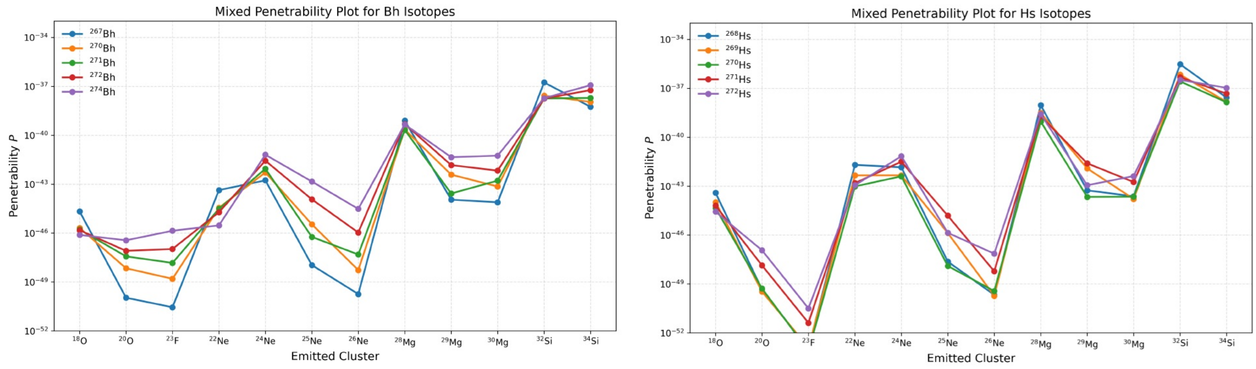

(a) Bohrium isotopes (b) Hassium isotopes

Figure 3: Collective penetration probability distributions for (a) ^{267,270,271,272,274}Bh and (b) ^{268,269,270,271,272}Hs, illustrating consistent structural preferences across isotopic series. Silicon clusters dominate due to their magic or near-magic nature, while magnesium clusters show secondary maxima corresponding to transitional shell structures.

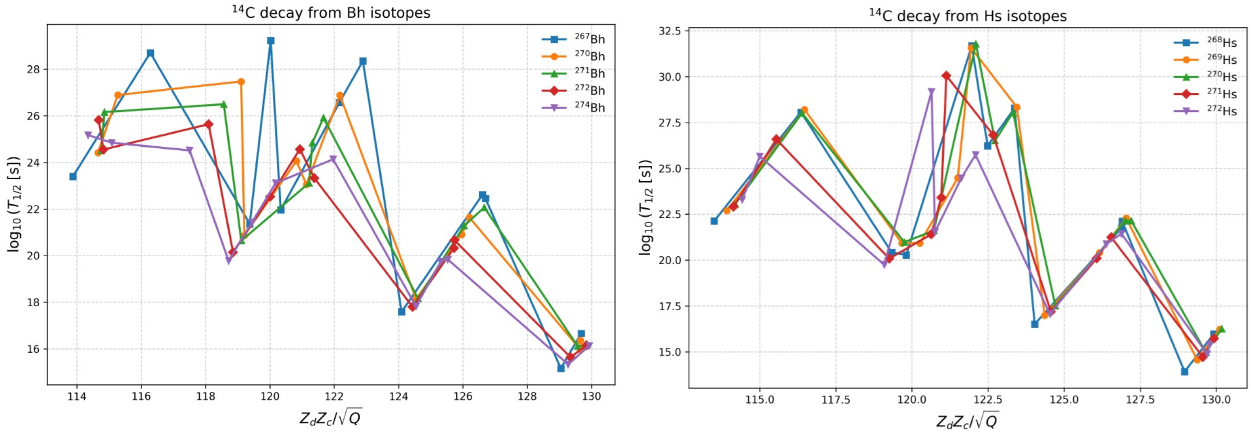

(a) Bohrium isotopes (b) Hassium isotopes

Figure 4: Geiger-Nuttall plots showing $\log_{10}(T_{1/2})$ versus $Z_d Z_c/\sqrt{Q}$ for (a) Bh and (b) Hs isotopes. The cluster-specific linear trends demonstrate the universal tunneling dependence, while systematic offsets between different cluster types reveal underlying nuclear structure effects, particularly for magic and near-magic clusters.

3.4 Remarks on Theoretical Uncertainties

The calculated half-lives are obtained within the WKB approximation and therefore depend on the input quantities entering the barrier penetration calculation. Among these, the decay energy (Q-value) is expected to have the most significant influence, since it directly determines the barrier penetrability. Additional sensitivity may arise from the adopted interaction potential and the associated model parameters. In the present work, however, all parameters of the Akyüz–Winther potential were adopted directly from the original literature without any modification or parameter adjustment, while the nuclear mass excesses were taken from the AME2020 evaluation (Wang et al., 2021). Consequently, the calculated half-lives represent predictions of the adopted theoretical framework using a consistent and fixed set of input parameters. Although a detailed quantitative uncertainty analysis has not been performed in the present study, the systematic trends discussed throughout this work are expected to remain reliable because all investigated decay channels were evaluated within the same theoretical formalism and under identical computational conditions.

4 Conclusions

In the present work, the cluster radioactivity of superheavy nuclei in the region $Z = 107$–108 (^{267,270,271,272,274}Bh and ^{268,269,270,271,272}Hs) has been systematically investigated within a binary decay framework. Particular attention was paid to the role of nuclear structure, including magic and near-magic configurations, and the evenodd character of the parent nuclei. Cluster radioactivity, first observed experimentally in heavy nuclei, is strongly influenced by shell effects and cluster stability (Rose and Jones, 1984).

The calculated decay properties, summarized in Tables 11 and 12, highlight clear structural effects. Heavier clusters, particularly ^{32}Si and ^{34}Si, consistently exhibit the shortest half-lives for both Bh and Hs isotopes

($T_{1/2} \sim 10^{14}$–10^{15} s), reflecting their enhanced Q-values, barrier penetrabilities, and favorable preformation probabilities due to near-magic ($N = 18$) and magic ($N = 20$) neutron numbers. Lighter clusters such as ^{18,20}O and $^{22-26}$Ne display significantly longer half-lives, emphasizing the stabilizing effect of shell closures on cluster emission.

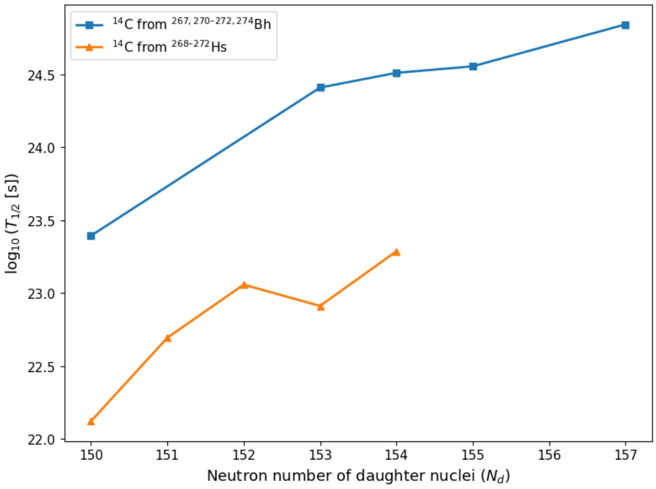

Figure 5: Representative half-lives for the emission of ^{14}C from the parent Bh and Hs nuclei, plotted as a function of the neutron number of the emitted cluster. This figure serves as a visual example of the systematics discussed in the text.

Table 11: Total half-lives of emitted clusters summed over all considered isotopes of Bh ($Z = 107$) and Hs ($Z = 108$). Clusters are ordered by increasing charge and mass.

Emitted Cluster	$T_{1/2}^{\text{total}}$ (Bh) [s]	$T_{1/2}^{\text{total}}$ (Hs) [s]
^{18}O	1.93×10^{23}	8.17×10^{21}
^{20}O	1.09×10^{25}	4.00×10^{25}
^{23}F	3.00×10^{24}	1.29×10^{29}
^{22}Ne	7.591×10^{21}	1.35×10^{20}
^{24}Ne	3.59×10^{19}	3.07×10^{19}
^{25}Ne	2.47×10^{21}	2.16×10^{23}
^{26}Ne	1.24×10^{23}	5.02×10^{25}
^{28}Mg	1.403×10^{17}	1.67×10^{16}
^{29}Mg	4.85×10^{19}	7.86×10^{19}
^{30}Mg	4.75×10^{19}	4.72×10^{20}
^{32}Si	9.95×10^{14}	5.22×10^{13}
^{34}Si	1.19×10^{15}	1.19×10^{15}

Table 12: Total half-lives of Bh and Hs isotopes obtained by summing the decay constants over all considered cluster-emission channels.

Element	Parent Isotope	$T_{1/2}^{\text{total}}$ (s)
Bh	^{267}Bh	1.40×10^{15}
Bh	^{270}Bh	6.68×10^{15}
Bh	^{271}Bh	6.75×10^{15}
Bh	^{272}Bh	3.31×10^{15}
Bh	^{274}Bh	1.85×10^{15}
Hs	^{268}Hs	8.17×10^{13}
Hs	^{269}Hs	3.54×10^{14}
Hs	^{270}Hs	8.88×10^{14}
Hs	^{271}Hs	4.73×10^{14}
Hs	^{272}Hs	5.74×10^{14}

The total half-lives of the parent isotopes (Table 12) further demonstrate the influence of nuclear structure: even-N nuclei, such as ^{272}Bh ($T_{1/2} = 3.31 \times 10^{15}$ s) and ^{268}Hs ($T_{1/2} = 8.17 \times 10^{13}$ s), exhibit the shortest overall half-lives across all clusters, reflecting the enhancement of decay probability in even-even systems. Hs isotopes systematically show shorter half-lives than Bh, consistent with their fully paired nucleons and the resulting higher tunneling likelihood.

While the general trends are derived from the comprehensive cluster calculations, Figure 5 illustrates a representative case for the emission of ^{14}C from the parent nuclei, demonstrating how half-lives vary with neutron number of the emitted daughter and serving as a visual example of the underlying systematics.

Overall, these results confirm that nuclear shell effects, magic and near-magic configurations, and the intrinsic structure of both parent and emitted nuclei govern the systematics of cluster radioactivity in the $Z = 107$–108 region. The dominance of ^{32,34}Si emissions, together with the observed evenodd trends in parent nuclei, provides a consistent framework to understand cluster decay behavior in superheavy systems, in agreement with previous theoretical and experimental studies (Poenaru et al., 2012; Jia et al., 2021).

Conflict of Interest

The authors declare no potential conflict of interest regarding the publication of this work.

Funding

The authors declare that no funds, grants, or other financial support were received during the preparation of this manuscript.

References

Akyuz, R. and Winther, A. (1979). Parameterization of the nucleus-nucleus potential. In *Proc. Enrico Fermi Int. School of Physics*, page 491.

Gales, S., Hourani, E., Hussonnois, M., et al. (1984). Exotic Nuclear Decay of Ra-223 by Emission of C-14 Nuclei. *Physical Review Letters*, 53(8):759.

Jia, J., Qian, Y., and Ren, Z. (2021). Possible cluster states in heavy and superheavy nuclei. *Physical Review C*, 104(3):L031301.

Langer, R. E. (1937). On the connection formulas and the solutions of the wave equation. *Physical Review*, 51(8):669.

Liu, J., Wang, Z., Zhang, H., et al. (2024). Theoretical predictions on cluster radioactivity of superheavy nuclei with Z= 119, 120. *Chinese Physics C*, 48(1):014105.

Pahlavani, M. and Babi, M. S. (2024). Study of the He-4, Be-10, C-14, N-14, and O-16 accompanied ternary fission of

Cf-248 isotope in the fragments equatorial geometry. *Chinese Journal of Physics*, 89:469–480.

Pahlavani, M. and Babi, M. S. (2025). Comparison of the equatorial and the collinear fragments geometry for Be-8, Si-28, Ni-58, and Zr-90 accompanied ternary fission of Fm-244 isotope. *Indian Journal of Physics*, 99(8):2993–3007.

Pahlavani, M. and Saeidi Babi, M. (2025). Comparison of light and heavy isobars obtained in the ternary fission of Fm-260 isotope in the equatorial and collinear geometries. *Pramana*, 99(3):128.

Pahlavani, M. and Saeidibabi, M. (2025). Study of the true ternary fission of Cf-248 isotope in equatorial and collinear geometries. *Chinese Physics C*, 49(7):074103.

Pahlavani, M. and Shamami, S. R. (2020). Clusters decay half-live of various heavy deformed nuclei with mass numbers in the range $221 \leq A \leq 242$. *Chinese Journal of Physics*, 66:733–744.

Poenaru, D., Gherghescu, R., and Greiner, W. (2012). Cluster decay of superheavy nuclei. *Physical Review CNuclear Physics*, 85(3):034615.

Poenaru, D. N. and Greiner, W. (2010a). Cluster radioactivity. In *Clusters in Nuclei: Volume 1*, pages 1–56. Springer.

Poenaru, D. N. and Greiner, W. (2010b). Cluster radioactivity. In *Clusters in Nuclei: Volume 1*, pages 1–56. Springer.

Rose, H. and Jones, G. (1984). A new kind of natural radioactivity. *Nature*, 307(5948):245–247.

Sandulescu, A., Poenaru, D., and Greiner, W. (1980). New type of decay of heavy nuclei intermediate between fission and. cap alpha. decay. *Sov. J. Particles Nucl.(Engl. Transl.);(United States)*, 11(6).

Santhosh, K. and Joseph, A. (2004). Cluster radioactivity in barium isotopes. *Indian Journal of Pure and Applied Physics*, 42.

Santhosh, K. and Priyanka, B. (2014). Probable cluster decays from 270–318118 superheavy nuclei. *International Journal of Modern Physics E*, 23(10):1450059.

Soylu, A., Sert, Y., Bayrak, O., et al. (2012). Role of the cluster deformations in explaining the exotic decay half-lives. *The European Physical Journal A*, 48(9):128.

Wang, M., Huang, W. J., Kondev, F. G., et al. (2021). The AME 2020 atomic mass evaluation (II). Tables, graphs and references. *Chinese Physics C*, 45(3):030003.

Warda, M., Zdeb, A., and Robledo, L. M. (2018). Cluster radioactivity in superheavy nuclei. *Physical Review C*, 98(4):041602.

Wei, K. and Zhang, H. F. (2020). α decay and cluster radioactivity within the redefined preformed cluster method. *Physical Review C*, 102(3):034318.

Zhang, G., Yao, Y., Guo, M., et al. (2016). Comparative studies for different proximity potentials applied to large cluster radioactivity of nuclei. *Nuclear Physics A*, 951:86–96.

To cite this article:

M. Azizi shamami, M. R. Pahlavani, M. Saeidi babi (2026). Cluster decay half-Lives for Bh and Hs superheavy isotopes in the mass region $A = 267$–274. *Radiation Physics and Engineering*, In Press.

DOI:

To link to this article: